A&A 622, A121 (2019)
https://doi.org/10.1051/0004-6361/201833678

Astronomy & Astrophysics

ARCiS framework for exoplanet atmospheres

The cloud transport model

Chris W. Ormel[1] and Michiel Min[2]

[1] Anton Pannekoek Institute (API), University of Amsterdam, Science Park 904, 1090 GE Amsterdam, The Netherlands
e-mail: c.w.ormel@uva.nl
[2] Netherlands Institute for Space Research (SRON), Sorbonnelaan 2, 3584 CA Utrecht, The Netherlands
e-mail: m.min@sron.nl

Received 19 June 2018 / Accepted 9 December 2018

ABSTRACT

Context. Understanding of clouds is instrumental in interpreting current and future spectroscopic observations of exoplanets. Modeling clouds consistently is complex, since it involves many facets of chemistry, nucleation theory, condensation physics, coagulation, and particle transport.
Aims. We aim to develop a simple physical model for cloud formation and transport, efficient and versatile enough that it can be used, in modular fashion for parameter optimization searches of exoplanet atmosphere spectra. In this work we present the cloud model and investigate the dependence of key parameters as the cloud diffusivity K and the nuclei injection rate $\dot{\Sigma}_n$ on the planet's observational characteristics.
Methods. The transport equations are formulated in 1D, accounting for sedimentation and diffusion. The grain size is obtained through a moment method. For simplicity, only one cloud species is considered and the nucleation rate is parametrized. From the resulting physical profiles we simulate transmission spectra covering the visual to mid-IR wavelength range.
Results. We apply our models toward KCl clouds in the atmosphere of GJ1214 b and toward $MgSiO_3$ clouds of a canonical hot-Jupiter. We find that larger K increases the thickness of the cloud, pushing the $\tau = 1$ surface to a lower pressure layer higher in the atmosphere. A larger nucleation rate also increases the cloud thickness while it suppresses the grain size. Coagulation is most important at high $\dot{\Sigma}_n$ and low K. We find that the investigated combinations of K and $\dot{\Sigma}_n$ greatly affect the transmission spectra in terms of the slope at near-IR wavelength (a proxy for grain size), the molecular features seen at approximately μm (which disappear for thick clouds, high in the atmosphere), and the 10 μm silicate feature, which becomes prominent for small grains high in the atmosphere.
Conclusions. Clouds have a major impact on the atmospheric characteristics of hot-Jupiters, and models as those presented here are necessary to reveal the underlying properties of exoplanet atmospheres. The result of our hybrid approach – aimed to provide a good balance between physical consistency and computational efficiency – is ideal toward interpreting (future) spectroscopic observations of exoplanets.

Key words. methods: numerical – planets and satellites: atmospheres – planets and satellites: composition

1. Introduction

The composition of exoplanet atmospheres contains very important clues to their formation and evolution. Different formation scenarios predict different abundances of key elements like C, O, N, and Si (e.g., Öberg et al. 2011; Helling et al. 2014; Mordasini et al. 2016; Madhusudhan et al. 2017). Measuring the abundances of these elements is one of the major goals of performing exoplanet atmosphere spectroscopy (see e.g., Brewer et al. 2017). With the launch of the *James Webb* Space Telescope (JWST) scheduled in 2021, a new wavelength window, the near- to mid-IR, will open up for compositional analysis of exoplanet atmospheres. With the recently selected ARIEL mission on the 2028 horizon, performing spectroscopy of a statistically significant sample of exoplanets, the future for atmosphere characterization looks particularly bright (Turrini et al. 2018). This new spectroscopic window presents us with many opportunities, but at the same time provides challenges in proper interpretation.

One of the major hurdles in atmospheric characterization is the presence of clouds obscuring the gaseous content of the atmosphere. Besides shielding the gaseous atmosphere from detection, clouds also alter the chemical composition of the gaseous atmosphere. By removing elements from the gas phase and raining them down to deeper layers, cloud processes alter the chemical composition of the atmosphere. For the interpretation of the atmosphere spectrum, this can lead to an incorrect assessment of the atomic composition of the bulk planet.

The difficulty of modeling cloud formation has led to a rich variety of different treatments of clouds. For models that retrieve key atmospheric parameters (temperature, pressure, and chemical profiles) directly from the observations, so-called retrieval models, it is very important that the simulations can be performed in the most computationally efficient manner. These methods often simply apply an atmospheric pressure below which the opacity of the atmosphere is gray (or infinite) with the possible addition of Rayleigh scattering haze (see e.g., Kreidberg et al. 2015; Barstow et al. 2017). This assumption might be acceptable for the narrow wavelength range considered in most studies right now. However, when the wavelength range extends, it becomes crucial to take into account the wavelength dependence of the optical properties of the cloud particles.

In forward models the complexity of the cloud formation varies. The approximate cloud formation model by Ackerman & Marley (2001) is probably one of the most widely used cloud

formation frameworks. In this model the physical properties of the cloud particles are parameterized in terms of a single parameter, $f_{\rm sed}$, the ratio between the particle sedimentation and the turbulent eddy velocities. It can be regarded as a proxy of the cloud particle size, although for constant $f_{\rm sed}$ the size will vary with height. While the assumption of a constant $f_{\rm sed}$ is not a priori evident, the advantage of this approach is that it avoids an elaborate grain microphysical prescription. At the other extreme are full self-consistent models that follow the microphysics of grain nucleation, condensation, transport and chemistry (Helling et al. 2008; Gao et al. 2018). Nevertheless, enhanced model complexity also introduces drawbacks. First, these models tend to be computationally demanding and are therefore not well suited for implementation in retrieval codes. In addition, increased model complexity often implies a great number of free parameters, which either need to be justified or else need to be explored, increasing the computational demand. Most crucially in this regard is the formation of condensation seeds (nucleation), which under the extreme conditions in exoplanet atmospheres is poorly understood. These considerations might argue in favor of building a retrieval framework that contains no cloud formation physics and, by fitting the spectrum, have the observations tell us what is going on (see e.g., Barstow et al. 2017; Tsiaras et al. 2018). While this is a widely used approach, a drawback of this approach is that it comes with a plethora of free parameters, which physical consistency is not a priori guaranteed (e.g., the feedback of cloud formation on the atmospheric composition is not necessarily accounted for).

Here, we aim for an intermediate approach, in which the cloud structure is computed in a simplified but consistent forward model. We envision that such a hybrid model has the benefits of both worlds: it should include the most elementary cloud physics (e.g., condensation and cloud transport) consistently, but yet be computationally fast and flexible enough to allow for parameter studies and incorporation in retrieval algorithms. Recent examples of this approach are the semi-analytical model by Charnay et al. (2018), applicable for Brown Dwarfs and young exoplanets, 1D dust coagulation models of atmospheres of planets embedded in their natal gas disk (Movshovitz et al. 2010; Mordasini 2014; Ormel 2014), and 1D cloud transport models for exoplanets (Ohno & Okuzumi 2017, 2018; Kawashima & Ikoma 2018). A common characteristics of these approaches is that they are one dimensional and consider a single, representative particle size that varies with height. In this paper we follow these lead to efficiently compute the formation of clouds for hot Jupiters. We use a diffusion/condensation framework to compute the growth of cloud particles and include particle coagulation. On the other hand, the nucleation rate is parameterized to accommodate the large uncertainty in nucleation efficiency.

The cloud model that we present in this paper will become part of a general framework for analysis and retrieval of exoplanet spectra[1]. In this context we are developing a code for computation of atmospheric properties, radiative transfer, and retrieval named ARCiS (ARtful modeling Code for exoplanet Science). The overarching aim of ARCiS is to develop an approach that is well-balanced between physical consistency, model complexity and computationally efficiency. The physical consistency allows for direct physical interpretation of observations. The modest model complexity allows for in depth understanding of the effects going on. The computational efficiency ensures that the model can be efficiently used in spectral retrieval analysis of observations. In this paper we focus on the cloud model; a validation of the entire ARCiS framework and subsequent fitting of real spectra will be deferred to upcoming studies.

In Sect. 2, the cloud formation model is explained. In Sect. 3, we present the resulting cloud structures and transmission spectra for a sub-Neptune (GJ1214 b) and for a typical hot-Jupiter planet, while varying the diffusivity and nucleation rate. In Sect. 4, we present the synthetic transmission spectra in the near- to mid-IR for the hot-Jupiter configuration. An assessment of the cloud model is proved in Sect. 5. In Sect. 6, we summarize the results and discuss extensions to this modeling framework.

2. Model

Our cloud particle model entails solving for the 1D steady-state solutions to the transport equations involving vapor, condensates, and nuclei. Cloud particles are initiated through nucleation at prescribed rates. Vapor can condense on these seeds and the particles may further grow by coagulation. Particles are transported by gravitational settling and turbulent (eddy) diffusion, until they reach the bottom of the cloud, hot enough to result in their evaporation. For simplicity a single species – KCl in case of GJ1214 b and $MgSiO_3$in case of the generic hot Jupiter – is considered. The choice for the species in question is arbitrary, although for the cloud to be observed, it must lie high in the atmosphere. Hence, the temperature of the upper atmosphere must be lower – but not much lower – than the condensation temperature. It is also straightforward to extend the model to include other chemical compounds.

2.1. Atmosphere model

We consider the atmosphere typical to a hot Jupiter planet. To obtain its physical structure – the temperature $T(z)$, pressure $P(z)$ and density $\rho(z)$ profiles – we adopt the atmosphere model of Guillot (2010) to obtain a relation between temperature and depth:

$$T^4 = \frac{3T_{\rm int}^4}{4}\left(\frac{2}{3}+\tau\right) + \frac{3T_{\rm irr}^4 f_{\rm irr}}{4}\left[\frac{2}{3}+\frac{1}{\gamma\sqrt{3}}+\left(\frac{\gamma}{\sqrt{3}}-\frac{1}{\gamma\sqrt{3}}\right)e^{-\gamma\tau\sqrt{3}}\right], \quad (1)$$

where the internal temperature $T_{\rm int}$ is a measure of the planet's internal heat flux $\sigma T_{\rm int}^4$ – the rate at which the planet cools – $T_{\rm irr}$ a measure of the heat flux received from the star, τ the optical depth at IR wavelengths, and $\gamma = \kappa_{\rm vis}/\kappa_{\rm IR}$ the ratio between the opacity at visual (irradiated) and IR (outgoing) wavelengths. The parameter $f_{\rm irr}$ specifies the distribution of the incoming flux over the planet ($f_{\rm irr} = 1/4$ for an equal distribution over the entire planet is used here). The irradiation temperature is defined $T_{\rm irr} = T_\star(R_{\rm p}/r_{\rm p})^2$ where $T_\star$ is the stellar (effective temperature), $R_{\rm p}$ the planet radius and $r_{\rm p}$ the distance to the host star. See Guillot (2010) for further discussion.

Employing this relation between T and τ, the hydrostatic balance, and the ideal gas law we obtain the temperature and density as function of pressure. (In particular, for constant $\kappa_{\rm IR}$, as we will use here, we have $P = g_z\tau/\kappa_{\rm IR}$.) Figure 1 provides the P–T and ρ–T structures resulting from the atmosphere model for our generic hot Jupiter model and GJ1214 b (parameters are discussed in Sect. 3 and listed in Table 1). From the temperature a saturation vapor density ($P_{\rm sat}$) can be calculated. Vapor is

[1] The cloud model, written in `python`, is publicly available at `http://www.exoclouds.com/`.

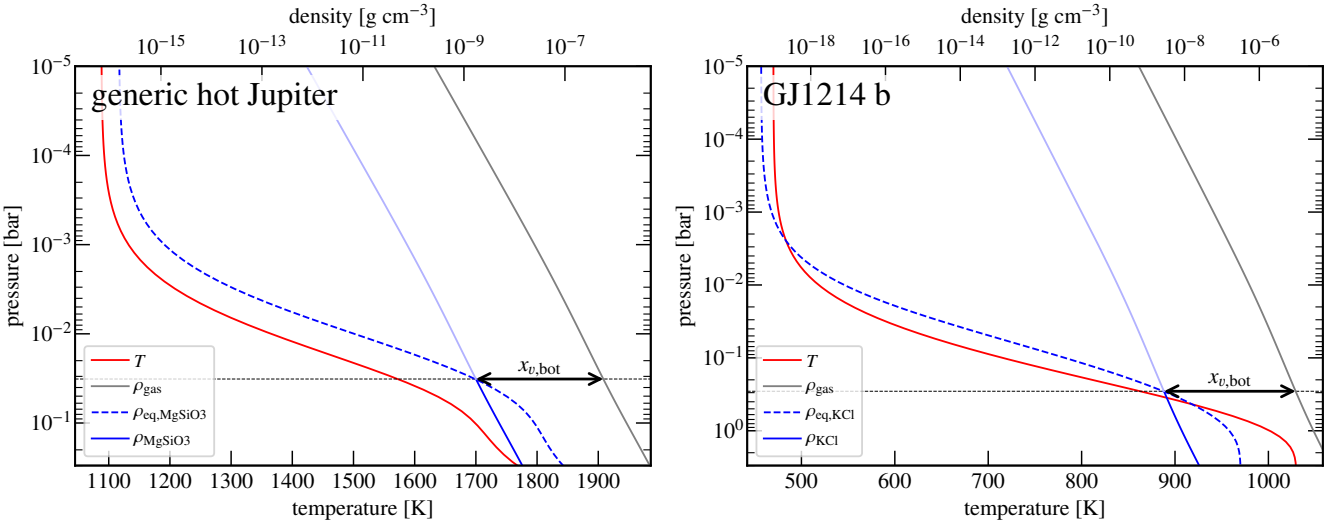

Fig. 1. *Left panel*: physical structure of a generic hot-Jupiter atmosphere. The temperature $T(P)$ and gas density profile $\rho_{\rm gas}(P)$ are obtained from the Guillot (2010) atmosphere model. The equilibrium density $\rho_{\rm eq}$ of $MgSiO_3$ is obtained from Eq. (18). Below the cloud deck (horizontal dashed line), $\rho_v = \rho(MgSiO_3) < \rho_{\rm eq}$; the species are present at constant abundance, such that $x_v = \rho_v/\rho_{\rm gas} \equiv x_{\rm v,bot}$ is constant. Above the cloud base ($\rho_v > \rho_{\rm eq}$; light blue) cloud formation (not included in this figure) will reduce the vapor density at the expense of condensates. *Right panel*: same for KCl in the GJ1214 b atmosphere.

expected to condense out when the partial pressure will exceeds $P_{\rm sat}$. Here, we re-express this condition in terms of a density: condensation occurs when $\rho_{\rm eq} < \rho_v$, where $\rho_{\rm eq} = m_v P_{\rm sat}/k_{\rm B}T$, $\rho_v = x_v\rho$ the vapor density, $k_{\rm B}$ Boltzmann constant, x_v the mass concentration, and m_v the molecular weight of the vapor species.

Let us denote the vapor concentration below the cloud deck by $x_{\rm v,bot}$. Below the cloud deck we can expect that $x_{\rm v,bot}$ is constant. The vapor density below the cloud deck is then simply $\rho_v = x_{\rm v,bot}\rho_{\rm gas}$ (blue line in Fig. 1). The height where $\rho_v = \rho_{\rm eq}$ (vertical dashed line) can be taken as the point where cloud formation starts – the base of the cloud. Because of transport effects it is conceivable that the cloud will extend below this height, for example, heavy rain particles take time to evaporate. Conversely, the cloud deck could be located at a higher layer if cloud formation requires strong, super-saturated conditions. These considerations are automatically accounted for in our numerical model.

Above the cloud base the vapor concentration is expected to become less than $x_{\rm v,bot}$ (light blue line) due to cloud formation. The surface (top) of the cloud is defined where the concentration of condensates $x_c = \rho_c/\rho_{\rm gas}$ is (close to) zero. The height where this occurs is not a priori known.

2.2. Cloud transport model

We model cloud transport of particles and vapor as advection-diffusion processes, solving equations like

$$\frac{\partial \rho_i}{\partial t} + \nabla \cdot \mathcal{M}_i = \mathcal{S}_i, \tag{2}$$

where ρ_i is the mass density of a certain species i, t is time, and $\mathcal{M}_i$ the mass flux

$$\mathcal{M}_i \equiv \rho_i \boldsymbol{v}_{{\rm sed},i} - \mathbf{K}\rho_{\rm gas}\nabla x_i, \tag{3}$$

x_i the mass concentration of species i, $v_{{\rm sed},i}$ the particle sedimentation velocity, $\mathbf{K}$ the diffusion tensor, and $\rho_{\rm gas}$ the gas density. In this work, we consider only vertical (z) transport, implying that only one velocity component and one diffusion element (K_{zz}) remain ($\boldsymbol{v}_{\rm sed} = 0$ for a vapor species). The RHS of Eq. (2), $\mathcal{S}_i$, specifies source terms arising from deposition (condensation), sublimation (evaporation) or nucleation, depending on the species i. The sedimentation velocity is obtained by equating the aerodynamic drag force with the planet's gravity, $v_{\rm sed,p} = g_z t_{\rm stop}$ where $t_{\rm stop}$ encapsulates the aerodynamic properties of the cloud particle. In general, the gas drag force is non-linear in particle-gas velocity $v_{\rm sed}$ (see e.g., Whipple 1972) and $t_{\rm stop}$ must be found by iteration. However, for small particles $t_{\rm stop}$ becomes independent of velocity. In particular, for the parameters of our model cloud, the gas drag law obeys the Epstein (1924) regime (free molecular flow) for which

$$t_{\rm stop-Epstein} = \frac{a_p \rho_\bullet}{v_{\rm th}\rho_{\rm gas}}, \tag{4}$$

where a_p is the radius of the grain, $\rho_\bullet$ its internal density, $v_{\rm th} = \sqrt{8k_{\rm B}T/\pi m_{\rm gas}}$ the thermal velocity of the gas. The Epstein drag law applies in the free molecular flow regime, $a_p < \frac{9}{4} l_{\rm mfp}$, where $l_{\rm mfp} = m_{\rm gas}/(\sqrt{2}\rho_{\rm gas}\sigma_{\rm mol})$ is the mean free path.

We employ the following assumptions:

1. The medium consist of three components – nuclei (n), condensates (c), and vapor (v). Only a single cloud species is considered. Any gas–gas or gas–grain chemistry is not accounted for.
2. The model is plane parallel; only the vertical dimension (z) is modeled and the only relevant diffusion coefficient is K_{zz}.
3. The cloud model is in steady state, $\partial/\partial t = 0$. This implies that
$$\mathcal{M}_v = -\mathcal{M}_c \tag{5}$$
at any location.
4. Nucleation is parametrized in the form of a log-normal profile with height (pressure)
$$\mathcal{S}_n = \rho_{\rm gas} g_z \frac{\dot{\Sigma}_N}{\sigma_* P\sqrt{2\pi}} \exp\left[-\frac{1}{2\sigma_*^2}\left(\log\frac{P}{P_*}\right)^2\right], \tag{6}$$
where $\dot{\Sigma}_N$, P_* and σ_*, respectively, indicate the integrated nuclei production rate, the characteristic height where the nuclei are deposited, and the width of the distribution.

Table 1. Cloud and atmospheric parameters for the generic hot-Jupiter and GJ1214 b.

Symbol	(default) Value		Unit	Description
	Generic HJ	GJ1214 b[a]		
Species	$MgSiO_3$	KCl		Cloud species
$\dot{\Sigma}_n$	$10^{-19}, 10^{-15}, 10^{-11}$		g cm^{-2} s^{-1}	Nucleation rate
γ	0.158	0.038		Opacity ratio visual and IR wavelengths (Eq. (1))
κ_{IR}	0.3	0.03	cm^2 g^{-1}	IR opacity
$\rho_\bullet$	2.8	2.8	g cm^{-3}	Particle internal density
σ_*	0.2			Width of nucleation profile (Eq. (6)).
σ_{com}	8×10^{-15}		cm^2	Combined (vapor and gas) molecular cross section
σ_{mol}	2×10^{-15}		cm^2	Molecular cross section (gas)
K_g, K_p	$10^6, 10^8, 10^{10}$	10^8	cm^2 s^{-1}	Particle and gas diffusivity
M_{planet}	1	0.0206	M_J	Planet mass
P_*	60	10^4	dyn cm^{-2}	Reference height for the nucleation profile (Eq. (6))
R_{pl}	1.087	0.244	R_J	Planet radius
$R_\star$	1	0.2064	$R_\odot$	Stellar radius
$T_\star$	5778	3026	K	Stellar effective temperature
T_{int}	500	60	K	Internal temperature
a_n	0.001		μm	Particle nucleation radius
f_{irr}	0.25			Heat distribution factor
f_{stick}	1.0			Vapor sticking probability
g_z	2192	893	cm s^{-2}	Gravitational acceleration
m_{gas}	2.34		m_H	Mean molecular weight (gas)
m_v	34.67	74.45	m_H	Mass vapor species
r_p	0.05	0.0143	au	Distance to star
$x_{v,bot}$	3×10^{-3}	3×10^{-4}		Vapor mass concentration at/below cloud base

Notes. [(a)]Empty entries indicate the value listed in the generic hot Jupiter column is used.

5. At any layer, the characteristic particle mass m_p is obtained taking the ratio of the total solid density of the particles (the density of condensates $\rho_c = x_c\rho_{gas}$ plus the density of nuclei $x_n\rho_{gas}$) to the particle number density n_p. In our model, the particle number density follows from the nuclei number density. In the case without coagulation any particle will contain only one nuclei, $n_p = n_n$ (below, in Sect. 2.3 this assumption will be relaxed, accounting for coagulation effects.) Hence,

$$m_p = \frac{(x_c + x_n)\rho_{gas}}{n_p} \approx \frac{x_c\rho_{gas}}{n_n} = \frac{x_c m_{n0}}{x_n}, \tag{7}$$

where m_{n0} is the mass of a single nuclei. In Eq. (7) the second step assumes that the condensates dominate the mass and the last step employs the single nuclei per cloud particle assumption: $n_n m_{n0} = x_n\rho_{gas}$. From the characteristic particle mass m_p a characteristic grain radius a_p follows, assuming that the grains are spherical. A grain size distribution is not accounted for, but it may be reconstructed from a_p. In addition, a_p changes with height through nucleation, condensation, evaporation, and coagulation. The grain radius a_p in turn determines the sedimentation velocity $v_{sed,p}$ of the particles.

6. We take the diffusivity (K_{zz}) equal for vapor and particles and independent of height. (These assumptions are easily relaxed, though).

We then obtain the following set of ordinary equations specifying the evolution of the condensate, nuclei, and vapor:

$$\frac{\partial \mathcal{M}_c}{\partial z} = \mathcal{S}_c, \tag{8a}$$

$$\frac{\partial \mathcal{M}_n}{\partial z} = \mathcal{S}_n, \tag{8b}$$

$$\frac{\partial x_c}{\partial z} = \frac{x_c v_{sed,p}}{K_{zz}} - \frac{\mathcal{M}_c}{K_{zz}\rho_{gas}}, \tag{8c}$$

$$\frac{\partial x_n}{\partial z} = \frac{x_n v_{sed,p}}{K_{zz}} - \frac{\mathcal{M}_n}{K_{zz}\rho_{gas}}, \tag{8d}$$

$$\frac{\partial x_v}{\partial z} = -\frac{\mathcal{M}_v}{K_{zz}\rho_{gas}}, \tag{8e}$$

where $\mathcal{M}_v$ is given by Eq. (5), $\mathcal{S}_n$ by Eq. (6), and the particle properties follow from x_c and x_n as described above.

The condensation rate $\mathcal{S}_c$ is given by

$$\mathcal{S}_c = f_{stick}(x_v\rho_{gas} - \rho_{eq}) \times \min\left[\pi a_p^2 v_{th,v} n_p; 4\pi a_p D_i n_p\right], \tag{9}$$

where D_i the diffusivity and f_{stick} a sticking probability, here taken unity, and $\rho_{eq} = m_v P_{sat}/k_B T$ the equilibrium (or saturation) density. Equation (9) combines the free molecular flow (vapor molecules travel on ballistic trajectories on the scale of the particle) and the diffusion-limited regimes (Woitke & Helling 2003; Yau & Rogers 1996). In Eq. (9) we have not accounted for the (liberated) latent heat of condensation.

For the diffusivity we follow Woitke & Helling (2003), after Jeans (1967), and write

$$D_i = \frac{k_B T}{3 P_{gas}\sigma_{com}} v_{th,red}. \tag{10}$$

This equation describes diffusion of a quantity in a two component medium of vapor and hydrogen gas. The reduced

thermal velocity $v_{\rm th,red}$ is taken equal to the mean gas thermal velocity ($v_{\rm th,red} = v_{\rm th}$) and $\sigma_{\rm com}$ is the combined cross section. We take, somewhat arbitrarily, $\sigma_{\rm com} = 8 \times 10^{-15}$ cm^2.

2.3. Adding coagulation

Coagulation among the cloud particles will decrease their number density n_p, relaxing the identity $n_p = n_n$, while leaving unaffected the mass concentration of nuclei. That is, coagulation will result in $n_p < x_n \rho_{\rm gas}/m_{\rm n0}$. Within the above framework, it is possible to include coagulation among the cloud particles by adding two additional equations, describing n_p:

$$\frac{\partial \mathcal{N}_p}{\partial z} = \frac{\mathcal{S}_n}{m_{\rm n0}} - \frac{n_p}{t_{\rm coag}}, \tag{11a}$$

$$\frac{\partial c_p}{\partial z} = c_p v_{\rm sed,p}/K_p - \mathcal{N}_p/K_p n_{\rm gas}, \tag{11b}$$

where $\mathcal{N}_p$ is the particle number flux and $t_{\rm coag}$ is the coagulation timescale, $c_p = n_p/n_{\rm gas}$ the particle concentration (by number), and $n_{\rm gas}$ the gas number density. The coagulation time includes contributions from differential settling (Δv) and Brownian motion. In terms of the coagulation rate ($\mathrm{d}n_p/\mathrm{d}t = -n_p/t_{\rm coag}$) these can be added:

$$t_{\rm coag}^{-1} = \frac{1}{2} n_p \pi (2a_p)^2 \Delta v + \frac{1}{2} 4\pi \min(v_{\rm BM} a_p, D_p) a_p n_p, \tag{12}$$

where $v_{\rm BM} = \sqrt{16 k_{\rm B} T/\pi m_p}$ for equal mass particles, $D_p = k_{\rm B} T/6\pi\eta a_p$ (Stokes-Einstein equation), $\eta = \nu_{\rm mol}\rho_{\rm gas}$ the dynamic viscosity, $\nu_{\rm mol} = 0.5 l_{\rm mfp} v_{\rm th}$ the molecular viscosity (Chapman & Cowling 1970), and Δv is the relative velocity between the cloud particles. The factor $\frac{1}{2}$ prevents double counting. Following Krijt et al. (2016) and Sato et al. (2016) it is appropriate to take $\Delta v = 0.5 v_{\rm sed}$ when the coagulation is driven by sedimentation. For identical particles having the same aerodynamical properties $\Delta v = 0$, but in reality a distribution in aerodynamical properties always ensures that $\Delta v \sim v_{\rm sed}$ (Okuzumi et al. 2011).

Adding these equations would bring the total number of equations to solve to seven. However, when we assume (correctly) that the nuclei mass is insignificant, $x_n \ll x_c$, there is no need to follow the nuclei mass density x_n. Equations (11a) and (11b) then replace Eqs. (8b) and (8d). To keep the expressions in units of mass concentrations (like x) and mass flux (like $\mathcal{M}$), we transform Eq. (11) by defining:

$$\tilde{\mathcal{M}}_n = m_{n0} \mathcal{N}_p, \tag{13a}$$

$$\tilde{x}_n = n_p m_{n0}/\rho_{\rm gas}. \tag{13b}$$

In terms of these new variables, Eq. (11) read

$$\frac{\partial \tilde{\mathcal{M}}_n}{\partial z} = \mathcal{S}_n - \frac{\tilde{x}_n \rho_{\rm gas}}{t_{\rm coag}}, \tag{14a}$$

$$\frac{\partial \tilde{x}_n}{\partial z} = \tilde{x}_n v_{\rm sed,p}/K_p - \tilde{\mathcal{M}}_n/K_p \rho_{\rm gas}. \tag{14b}$$

These are identical to Eqs. (8b) and (8d), except for the term involving $t_{\rm coag}$. In runs including coagulation we simply use these equations to follow the number density of nuclei (n_n or $\tilde{x}_n$). The nuclei mass density (x_n) is not followed, but this is justified since it is in any case negligible compared to the mass density of the condensate (x_c) and therefore bears no influence on the physical properties of the cloud particles.

2.4. Boundary conditions and solution technique

Equations (8a)–(8e) constitute a system of five first order, ordinary differential equations and five unknowns ($x_c, x_n, x_v, \mathcal{M}_c, \mathcal{M}_n$). Therefore, five boundary conditions are necessary. We specify boundary conditions at the bottom and the top of the domain. At the top of the cloud ($z = z_{\rm top}$) we demand that the condensate flux vanishes:

$$\mathcal{M}_c(z_{\rm top}) = 0 \tag{15}$$

and that the nuclei flux equals

$$\mathcal{M}_n(z_{\rm top}) = -\int_{z_{\rm top}}^{\infty} \mathcal{S}_n \mathrm{d}z, \tag{16}$$

while at the base of the cloud we put constraints on the mass concentrations:

$$x_n(z_{\rm bot}) = x_c(z_{\rm bot}) = 0; \quad x_v(z_{\rm bot}) = x_{\rm v,bot}. \tag{17}$$

The condition $x_c = 0$ reflects that at the base of the cloud the temperature has become high enough for all the condensates to be evaporated. The vapor concentration at the cloud base ($x_{\rm v,bot}$) is an input. The nuclei boundary condition $x_n = 0$ strictly only holds when the nuclei are also made of $MgSiO_3$, such that they would also evaporate. But this is not necessarily the case. Formally, we should extend the systems of equations describing evaporation of the nuclei species, which is a rather cumbersome extension of the model. Alternatively, we could introduce a free parameter for $n_n(z_{\rm bot})$. But we found its effects rather insignificant as long as it is not too large. Hence, we considered the simple choice of a zero concentration nuclei boundary condition is preferable above an (arbitrary) specification of the nuclei seed.

Since conditions are placed on both the upper and the lower boundary, Eqs. (8a)–(8e) represent a boundary value problem (BVP). This BVP is solved using the `solve_bvp` function from python's `SciPy` module (Ascher et al. 1994; Kierzenka & Shampine 2001; Shampine et al. 2006). These codes require an initial "guess" for the solution, which must be sufficiently close to the actual solution. Otherwise, convergence is not guaranteed. This represents a problem since the actual solution is of course unknown.

We therefore resort to an iterative approach, introducing a parameter ϵ that is added to the condensation rate $\mathcal{S}_c$ and the nucleation rate $\mathcal{S}_n$. Hence, $\epsilon = 0$ corresponds to the cloud-free solution ($x_v = x_{\rm v,bot}$, $x_c = 0$, $\mathcal{M}_c = 0$). Then, a very small ϵ, for example $\epsilon = 10^{-8}$, will give a solution that will be close to the known (cloud-free) solution that `solve_bvp` is able to solve. This new solution (with $\epsilon = 10^{-8}$) then provides the guess for the next iteration, where ϵ is larger. We progressively increase ϵ until $\epsilon = 1$, with which the desired cloud profiles are obtained.

A similar iterative approach can be designed for the boundaries of the domain. Although the bottom boundary is given by the $\rho_{\rm v,bot}$ constraint[2], the upper boundary is in principle open, as diffusion always allows some particles to be transported to the very upper regions. As a final step, we therefore adjust the boundaries of the domain, searching for a solution where x_c stays positive in the entire domain, while x_c near the boundary is a very tiny fraction (e.g., 10^{-8}) of its peak value.

With these incremental approach of "relaxing" to the solution, `solve_bvp` is still computational efficient. The 24 runs listed in Table 2 took an average of 17 s to complete on a modern desktop PC, with the slowest one requiring 25 s.

[2] The lower boundary may deviated from the $\rho_{\rm v,bot} = \rho_{\rm eq}$ condition when transport timescales are shorter than evaporation times, e.g., when the particles have become large and settle quickly.

Table 2. Table of output quantities.

Planet	Coagulation	K_{zz} ($cm^2\,s^{-1}$)	$\dot{\Sigma}_n$ ($g\,cm^{-2}\,s^{-1}$)	$\mathcal{M}_{c,max}$ ($g\,cm^{-2}\,s^{-1}$)	$P_{\tau=1}$ (bar)	$\tau_{z,tot}$	a_{max} (μm)
Generic HJ	×	10^{10}	10^{-11}	-1.8×10^{-6}	4.3×10^{-7}	3.0×10^{3}	0.051
	✓	10^{10}	10^{-11}	-1.7×10^{-6}	9.5×10^{-7}	740	0.24
	×	10^{10}	10^{-15}	-1.6×10^{-6}	8.9×10^{-6}	140	1.0
	✓	10^{10}	10^{-15}	-1.8×10^{-6}	1.0×10^{-5}	73	2.4
	×	10^{10}	10^{-19}	-1.3×10^{-6}	2.6×10^{-4}	5.0	20
	✓	10^{10}	10^{-19}	-1.3×10^{-6}	2.7×10^{-4}	3.9	26
	×	10^{8}	10^{-11}	-1.9×10^{-8}	3.5×10^{-6}	1.3×10^{4}	0.012
	✓	10^{8}	10^{-11}	-1.8×10^{-8}	1.9×10^{-5}	29	3.9
	×	10^{8}	10^{-15}	-1.9×10^{-8}	3.6×10^{-5}	460	0.25
	✓	10^{8}	10^{-15}	-1.8×10^{-8}	4.6×10^{-5}	22	4.1
	×	10^{8}	10^{-19}	-1.8×10^{-8}	2.1×10^{-3}	4.6	5.2
	✓	10^{8}	10^{-19}	-1.8×10^{-8}	2.1×10^{-3}	2.5	8.7
	×	10^{6}	10^{-11}	-1.9×10^{-10}	1.0×10^{-4}	6.2×10^{4}	2.7×10^{-3}
	✓	10^{6}	10^{-11}	-1.9×10^{-10}	6.6×10^{-4}	1.7	1.4
	×	10^{6}	10^{-15}	-1.9×10^{-10}	2.2×10^{-4}	450	0.058
	✓	10^{6}	10^{-15}	-1.9×10^{-10}	3.8×10^{-3}	1.6	1.3
	×	10^{6}	10^{-19}	-1.9×10^{-10}	5.6×10^{-3}	1.3	1.2
	✓	10^{6}	10^{-19}	-1.9×10^{-10}	5.8×10^{-3}	0.86	1.7
GJ1214 b	×	10^{8}	10^{-11}	-3.2×10^{-8}	5.6×10^{-6}	2.7×10^{4}	0.015
	✓	10^{8}	10^{-11}	-3.0×10^{-8}	2.0×10^{-4}	810	1.3
	×	10^{8}	10^{-15}	-3.1×10^{-8}	1.2×10^{-4}	1.2×10^{3}	0.30
	✓	10^{8}	10^{-15}	-3.0×10^{-8}	4.1×10^{-4}	250	2.5
	✓	10^{8}	10^{-19}	-2.7×10^{-8}	3.0×10^{-3}	16	17
	×	10^{8}	10^{-19}	-2.9×10^{-8}	2.5×10^{-3}	44	6.0

Notes. The first four columns list the input parameters: the planet (see Table 1 for parameters), whether coagulation is included or not, the diffusivity K_{zz}, and the nuclei production rate $\dot{\Sigma}_n$. The model calculates a steady-state cloud and we list: the peak mass flux (intensity of the rain) $\mathcal{M}_{c,max}$, the pressure level where the geometrical transmission optical depth reaches unity $P_{\tau=1}$, the total geometrical vertical optical depth of the cloud $\tau_{z,tot}$, and the maximum grain radius a_{max}.

3. Physical structure

In this section, we present the outcome of the cloud model in terms of its physical structure: the concentration and properties of the cloud particles. In Sect. 3.1, we consider a generic hot Jupiter planet, whereas in Sect. 3.2, we apply our model toward GJ1214 b to compare our results to previous findings.

3.1. Hot-Jupiter $MgSiO_3$ clouds

We consider a generic hot Jupiter planet situated at a distance of 0.05 au around a solar-like star. We consider $MgSiO_3$ as our cloud species, for which we use the saturation pressure of Ackerman & Marley (2001)

$$P_{sat} = 1.04\times10^{17}\exp\left[-\frac{58\,663}{T}\right]\mathrm{dyn\,cm^{-2}}. \quad (18)$$

Because $MgSiO_3$ does not exist in vapor phase, it would be erroneous to consider taking the molecular weight of $MgSiO_3$ (100.4 m_H) for m_v. Instead, we consider an effective vapor mass, which is given by the constituents from which $MgSiO_3$ forms. Typically, $MgSiO_3$ falls apart into three molecules (Helling et al. 2008). We therefore simply take $m_v = m_{MgSiO_3}/3 = 33.5\,m_H$. For the atmospheric parameters, we adopt parameters similar values as Line et al. (2013), see Table 1. An internal temperature of $T_{int} = 500$ K is used and an atmosphere IR-opacity of $0.3\,cm^2\,g^{-1}$. The higher IR-opacity crudely reflects the appearance of clouds; the model does presently not treat (thermal) feedback of the clouds on the profiles consistently. We have verified that changing these parameters does not affect the conclusions of this work. The corresponding atmospheric physical structure was shown in Fig. 1.

The outcome of the cloud model for the parameters listed in Table 1 is presented in Fig. 2 for the default model. In Fig. 3 we take eight other parameter combinations of K_{zz} and $\dot{\Sigma}_n$, crudely corresponding what has been used in literature studies (e.g., Kawashima & Ikoma 2018). Several output quantities of the runs are further listed in Table 2. The intensity of the rain is characterized by the mass flux parameter $\mathcal{M}_c$ whose peak value is listed. A higher $\mathcal{M}_{c,max}$ reflects more vigorous mass transport; this parameter hence correlates with the diffusivity K_{zz}. For reference, a value of $\mathcal{M}_c = 10^{-7}\,g\,cm^{-2}\,s^{-1}$ amounts to a $MgSiO_3$ precipitation of 11 mm yr^{-1}. We calculate both the vertical optical depth

$$\tau_z(z) = \int_z^{z_{top}} n_p(z')\pi a_p^2(z')\mathrm{d}z' \quad (19)$$

as well as the transmission optical depth in the geometrical limit

$$\tau_{trans}(z) = \int_z^{z_{top}} n_p(z')\pi a_p^2(z')\sqrt{\frac{2R}{(z'-z)}}\mathrm{d}z', \quad (20)$$

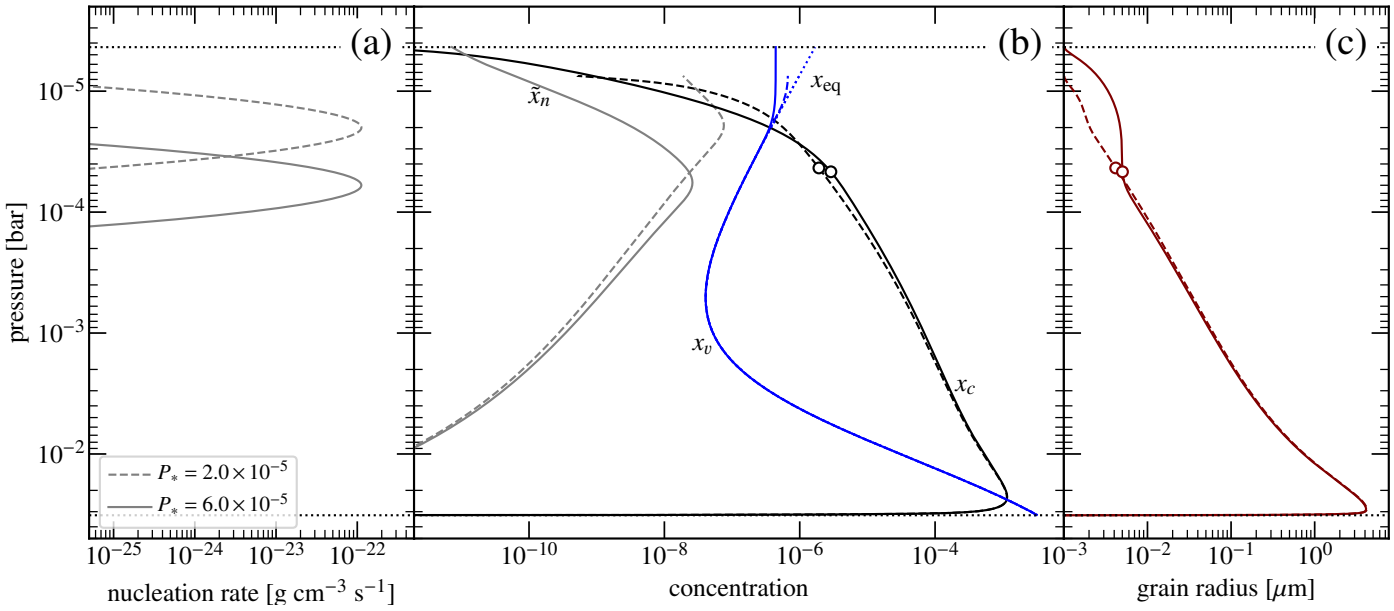

Fig. 2. Results of the standard model ($K = 10^8$ cm^2 s^{-1}; $\dot{\Sigma}_n = 10^{-15}$ g cm^{-2} s^{-1}). *Panel a*: nucleation rate $\mathcal{S}_n$, which follows a log-normal distribution around a reference pressure P_*. The dotted horizontal lines indicate the bottom and top of our computational domain. *Panel b*: concentrations of nuclei ($\tilde{x}_n$), condensates (x_c), and vapor (x_v). The equilibrium concentration corresponding to the saturation pressure is also plotted ($x_{\rm eq}$) but it virtually coincides with x_v. *Panel c*: characteristic grain radius a_p. The dashed lines correspond to a model where the nuclei are inserted at a higher layer than the standard. The open circles correspond to the depth where the geometrical transmission optical depth $\tau_{\rm trans}$ equals 1.

that is, the optical depth corresponding from the line perpendicular to height z. In Table 2 the total geometrical optical depth refers to τ_z as measured from the base of the cloud whereas the pressure level where τ reaches unity ($P_{\tau=1}$) refers to the transmission optical depth $\tau_{\rm trans}$. The latter quantity is more meaningful in the context of transmission spectra. These geometrical values only serve as a crude guide as opacities are not often close to their geometrical limit (especially for small particles). Proper simulated spectra are calculated in Sect. 4. Finally, we list the peak radius of the condensate particles, $a_{\rm max}$.

Figure 2 presents profiles of nucleation rate, concentrations of vapor condensates and nuclei and grain size for the standard model ($K_{zz} = 10^8$ cm^2 s^{-1}, $\dot{\Sigma}_n = 10^{-15}$ g cm^{-2} s^{-1}; the central panel of Fig. 3 corresponds to Fig. 2). Coagulation is included. Note the steep but continuous transition from cloudy to cloud-free near the bottom of the cloud. This is caused by the steep increase in the equilibrium density (Fig. 1). Several factors regulate the extent of the cloud. The first is the location where the nuclei form, which is given in Fig. 2a. Recall that the nuclei production profile $\mathcal{S}_n$ (Eq. (6)) is characterized by three parameters: P_*, σ_* and $\dot{\Sigma}_n$. In Fig. 2 we also present a case where the nuclei are released at a higher height (P_* is decreased by a factor three; dashed curves). Increasing the height where the nuclei are released does not much affect the profiles deeper in the atmosphere. In both cases cloud particles readily consume the vapor locally, whereas transport and coagulation act on larger (time)scales. However, there may be some observational consequences as the grain size around $\tau_{\rm trans} = 1$ is affected.

Comparing Figs. 2a and b, it can be seen that the height where nuclei are injected is also the height where the concentration of nuclei ($\tilde{x}_n$) peaks. Below this height $\tilde{x}_n$ decreases because particles' velocity speeds up due to their growth by condensation. The ratio of x_c and $\tilde{x}_n$ determines the size of the particles, which increases for our standard model to 4 μm just above the cloud base (Fig. 2c). In the upper regions, the particle radius levels off at $\approx$0.005 μm, several factors larger than the nucleation radius. Grains tend to be somewhat smaller and more abundant in the model where the nuclei are injected at a larger height, because they accrete less vapor before settling down (Figs. 2b and c). Although at these heights the density of $MgSiO_3$ is rather low, the larger grain size may be of some observational importance for the transmission spectra, especially concerning the Rayleigh scattering at optical wavelengths.

More important in regulating the cloud thickness is the eddy diffusivity K_{zz}. A larger K_{zz} implies that more vapor is transported upwards and that more (small) particles can be found above the nuclei injection height. This is illustrated in Fig. 3 where we vary the diffusivity (rows) and the total nucleation rate (columns). Clearly, larger diffusivity results in denser and thicker clouds; particles are uplifted to higher regions and more vapor is being transported from below the cloud deck. In the limit where the transport becomes dominated by diffusion, we can expect the concentration of condensates x_c to be identical to the concentration of the vapor at the base of the cloud, $x_{\rm v,bot} = 3\times10^{-3}$. This explains the boxy cloud profile of the $\dot{\Sigma}_n = 10^{-11}$, $K_{zz} = 10^{10}$ model (bottom right panel of Fig. 3).

Finally, we find that the cloud thickness increases with the nucleation rate $\dot{\Sigma}_n$ (Fig. 3). A higher $\dot{\Sigma}_n$ tends to reduce the grain size, since the total amount of vapor on a given grain is smaller when there are more of them. Since the grain size is a directly observational property, the nucleation model is therefore an essential part to any cloud model.

We also conducted runs without coagulation, in order to isolate its effects. These are presented by the dashed lines in Fig. 3. Clearly, coagulation does not affect the low $\dot{\Sigma}_n$ runs. The growth of particles in these runs is entirely due to condensation. Coagulation is more important at higher nucleation rates and for lower K_{zz}; the former because there is a larger surface available and the latter because the grains are more concentrated. The differences between the no-coagulation and coagulation runs are the greatest in the $(\dot{\Sigma}_n, K_{zz}) = (10^{-11}, 10^6)$ run (top right). The no-coagulation run is characterized by extremely small particles

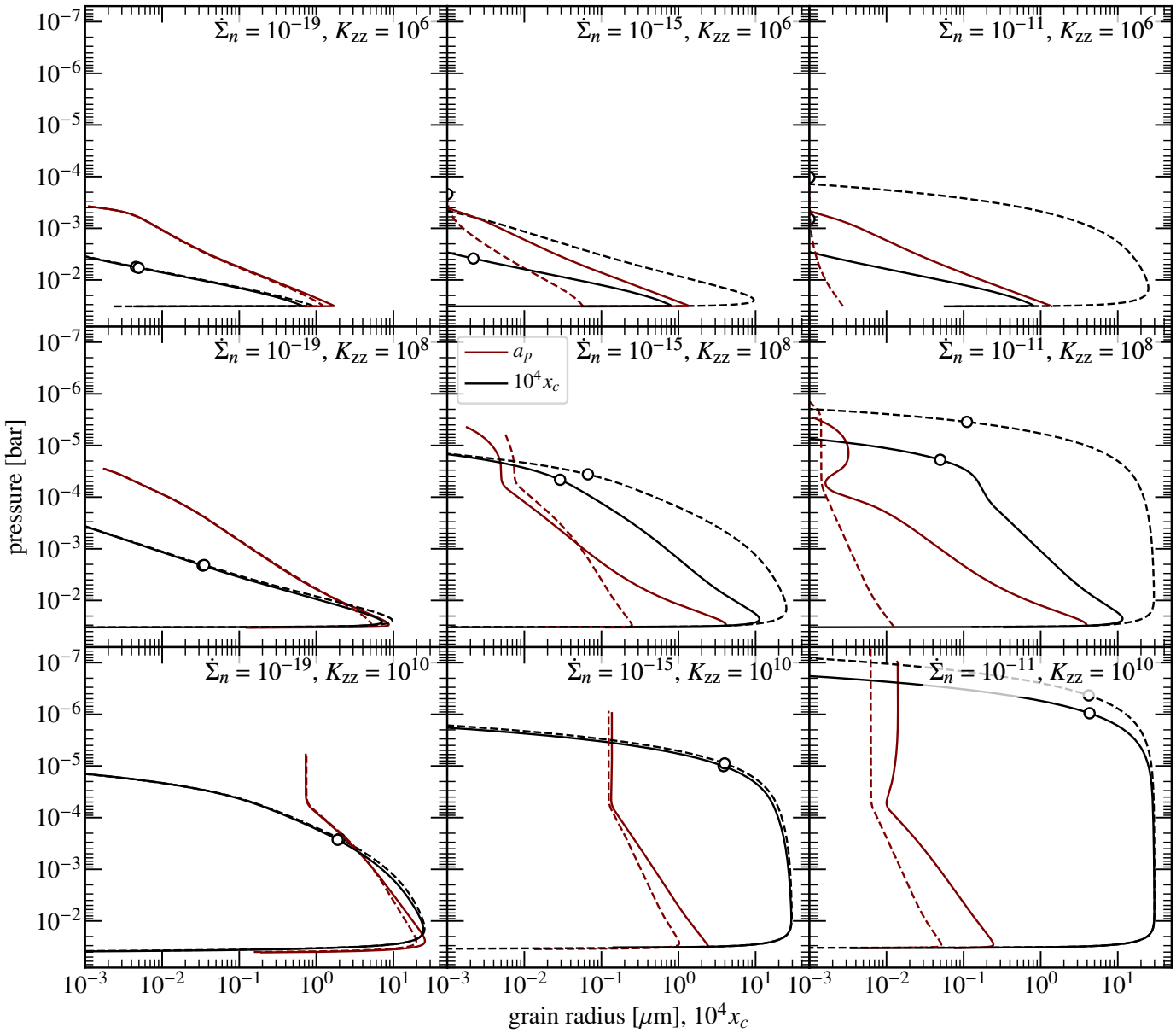

Fig. 3. Cloud profiles. The concentration of cloud particles (black) and the characteristic particle size (dark red; shared x-axis) against pressure, plotted for combinations of diffusivities K_{zz} and nucleation rates $\dot{\Sigma}_n$ (panels). The grain radius of particles in models without coagulation is shown by the dashed dark curve. The height where the transition optical depth reached unity ($\tau_{\rm trans} = 1$) is indicated by the circle.

(similar to the nucleation size) and the total geometrical optical depth of the cloud reaches values above 10^4 (see Table 2). Including coagulation, however, greatly increases the grain size, reducing the cloud vertical geometrical optical depth by over a factor of 10^4!

3.2. GJ1214 b KCl clouds

GJ1214 b is a super-Earth or sub-Neptune planet of radius $R_p = 2.7 \pm 0.1\,R_\oplus$ and mass $M_p = 6.5 \pm 1.0\,M_\oplus$ orbiting an M 4.5 star at a distance of 0.015 au (Charbonneau et al. 2009). With these bulk properties GJ1214 b could both a "water world" or a more standard terrestrial planet with a H/He envelope. Interestingly, GJ1214 b transmission spectra is virtually featureless (Kreidberg et al. 2014), indicative of clouds.

Cloud models have recently been applied to GJ1214 b (e.g., Gao & Benneke 2018; Ohno & Okuzumi 2018). Here we apply our cloud model toward GJ1214 b with the aim of comparing the physical structure (particle sizes and concentrations) against these works in the broadest sense. A detailed comparison, let alone a calibration, is rather meaningless as these works employ vastly different cloud microphysical and atmospheric models.

We consider KCl as our cloud species and use the $P_{\rm sat}$ profile presented in Morley et al. (2012). The concentration of KCl at the bottom of the atmosphere is taken to be $x_{v,\rm bot} = 3 \times 10^{-4}$. We largely follow Ohno & Okuzumi (2018) in choosing our atmospheric parameters (see Table 1). However, we keep $\kappa_{\rm IR}$ fixed; with $\kappa_{\rm IR} = 0.03\,{\rm cm^2\,g^{-1}}$ we obtain a P–T profile (Fig. 1) that resembles theirs. The diffusivity is fixed at $K_{zz} = 10^8\,{\rm cm^2\,s^{-1}}$ while we consider the same three values for the nuclei production rate $\dot{\Sigma}_n$. Nuclei are injected at a height corresponding to a pressure of 0.01 bar.

Results are shown in Fig. 4 where the particle radius is plotted against height for the three nucleation rates and for either

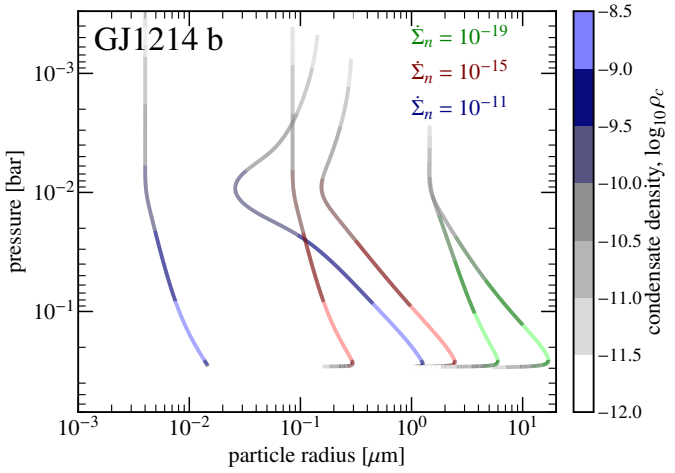

Fig. 4. Obtained particle size as function of pressure for the cloud models applied to GJ1214b. The intensity of the rain in terms of the volume density of condensates ($\rho_c = x_c\rho_{\rm gas}$) is indicated by the color bar. Three values of the nuclei production rate are considered (as indicated by color) and results are plotted with and without accounting for coagulation. The diffusivity parameter is fixed at $K_{zz} = 10^8\,{\rm cm^2\,s^{-1}}$. Particle radii are larger in runs that include coagulation.

the coagulation mode and the no-coagulation mode. The intensity of the rain in terms of the condensate volume density ρ_c is indicated by the color. The rain reaches its highest intensity near the cloud base. Clearly, the nuclear production rate – a free parameter in our model – has a key influence on the grain size. Also, it can be seen that clouds with the smallest grains are also the most extended, since these grains tend to diffuse, rather than settle. Finally, grains are larger in runs where coagulation is included. These findings reflect the discussion of the hot generic hot-Jupiter clouds in Sect. 3.1.

Comparing these curves to the $K_{zz} = 10^8\,{\rm cm^2\,s^{-1}}$, 1x solar metallicity panel of Fig. 5 of Gao & Benneke (2018), we see that their typical sizes of 1–10 μm correspond well to our results with the low $\dot{\Sigma}_n$. (In their model the nucleation rate is given by a full microphysical model.) The gradient in grain size with height seems to be a bit shallower in our models, however, considering that Gao & Benneke (2018) did not include coagulation.

Ohno & Okuzumi (2018) also modeled GJ1214 b and, like us, used a characteristic size approach. In addition, they too prescribed the nucleation. However, they fixed the nuclei number density at the cloud base. Compared to our choice of prescribing the entire profile, this has the advantage of only introducing a single free parameter. On the other hand, it results in the largest grains residing in the top of the cloud, which seems somewhat spurious. Their typical grain size of 1–2 μm nevertheless corresponds well to our results (they too account for coagulation) and their volume mixing ratios approach $x_c = 10^{-4}$ – the same as in our case.

4. Transmission spectra (hot Jupiter)

From Fig. 3 we see that the cloud thickness and particle size are heavily influenced by the diffusion strength and the nucleation rate. To investigate their effect on the spectral appearance of the transit signal of the planet, we computed for the nine cases of the generic hot-Jupiter model shown in Fig. 3 the transmission spectra. These are shown in Fig. 5.

To compute the spectra we have developed a radiative transfer tool for simulating exoplanet spectra. This code uses molecular line lists from the ExoMol project and the HITEMP and HITRAN databases to compute the molecular opacities with the method by Min (2017). A validation of this ARCiS module is given in Appendix A. Even though for the cloud condensation equations we use pure $MgSiO_3$ as a condensate, we add 10% of metallic iron to the particles when computing the optical properties. The implicit assumption is that the physical properties of the cloud particles (their sizes and concentrations) are well described by modeling the dominant condensate, in other words by our cloud model. However, this assumption cannot be made for the optical properties, which exhibit a strongly non-linear dependence on composition. $MgSiO_3$, for example, is completely transparent in the near-IR, while only a small fraction of iron in the silicate lattice, or condensed inclusions, like metallic iron, will suffice to give a significant near-IR opacity. Hence, lacking a multi species cloud model, we account for this by adding a small amount of continuum opacity in the form of metallic iron. The 10% metallic iron we take here is rather arbitrary and could be up to 50% given the cosmic abundance of iron. The true iron fraction in planetary atmospheres is a parameter that we have to derive from observations or constrain from planet formation theory.

The cloud opacities are computed using refractive index data from Jaeger et al. (1998) and Henning & Stognienko (1996) where we mix the iron and $MgSiO_3$ together using effective medium theory. We use the distribution of hollow spheres (DHS) method from Min et al. (2005) to convert the refractive index into particle optical properties. The gas phase chemistry is computed assuming thermochemical equilibrium using the code from Mollière et al. (2017). The atomic abundances that go into the chemical computations are assumed to be solar with depletions in Si, O, and Mg according to the computed value of x_v. This causes the C/O ratio to change in the cloud forming region, affecting the chemistry there. Below the cloud deck the C/O ratio is solar, C/O = 0.55, while in the cloud forming region C/O $\approx$ 0.7.

In Fig. 5 the mid-IR transmission spectra are plotted for the same combination of diffusivities and nucleation rate as in Fig. 3. The near- to mid-IR spectral region will become available with the MIRI instrument onboard JWST and further into the future with the recently selected ARIEL mission. Several inferences can be made. First, increasing the cloud thickness (either by increasing $\dot{\Sigma}_N$ or increasing K_{zz}) suppresses the molecular features of, for example, H_2O in the 1–3 μm range. The reason is that, the $\tau = 1$ height now resides much higher in the atmosphere to shield the molecular emission.

A striking result is the spectral appearance of $MgSiO_3$ around 10 μm. The 10 μm silicate resonance is very sensitive to particle size. Small particles give a strong resonance signature, while increasing the particle size, the signature is flattened (see e.g., Min et al. 2005). In addition, the solid feature stands out stronger against the (molecular) background for thicker clouds. Therefore, the resonance around 10 μm is most clearly seen in the case with high nucleation rate and diffusion strength (lower right panel), that is, a thick cloud of small particles. Only for the lowest diffusion strength (upper panels) does the silicate signature become unobservable around 10 μm. Finally, Fig. 5 displays a very interesting evolution of the slope of the near-IR signature. For the low nucleation rate models, the effect of increasing the cloud thickness (i.e., the diffusion strength) results in a gray near-IR spectrum. On the other hand, for the high nucleation rate, the near-IR spectrum is characterized by a much steeper slope. The reason behind this diverging trend with cloud thickness is the dependence of particle size with nucleation rate.

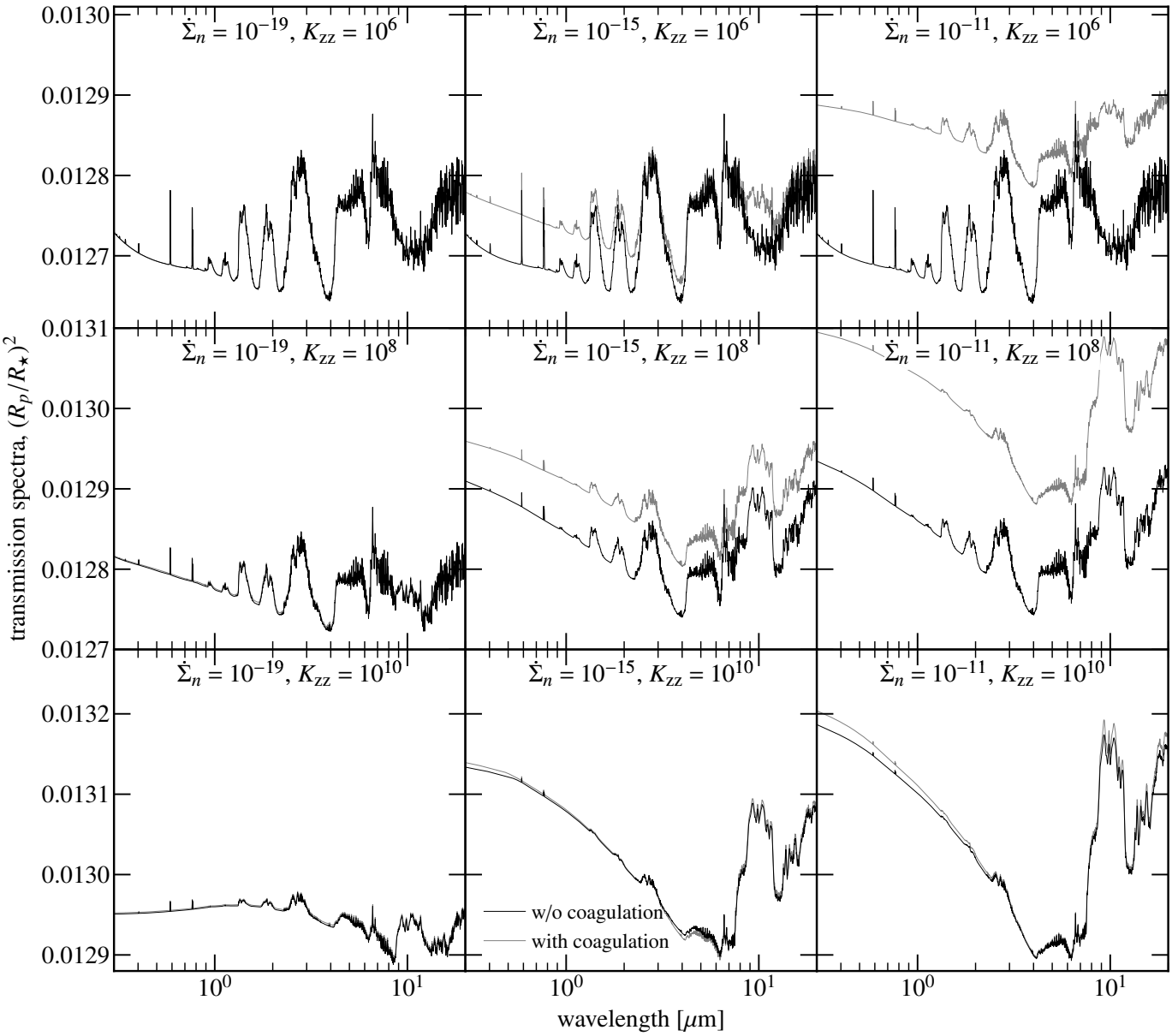

Fig. 5. ARCiS-Simulated transmission spectra corresponding to the physical profiles presented in Fig. 3 as function of wavelength. Gray curves give the spectra without accounting for coagulation, black curves include coagulation. The scaling of the y-axis is different for the different diffusivities (higher K_{zz} results in a larger R_p).

Higher nucleation rates result in smaller grains whose opacity has a much steeper wavelength dependence in the near-IR region. Conversely, the 1–10 μm grains that are produced in the low $\dot{\Sigma}_n$, high K run (bottom left panel) result in a gray opacity and a transmission spectra insensitive to wavelength.

The spectra we computed are sensitive to the effects of particle coagulation. The effects are twofold. One is that coagulation causes the grains to grow and settle deeper into the atmosphere. Second the opacity of the larger particles produced by coagulation is different. It can be seen that when we switch off the coagulation the cloud deck in the upper right four panels of Fig. 5 is much higher and thus mutes the molecular features more. In addition, the spectral appearance typical for small particles, the silicate feature at 10 μm and the Rayleigh scattering slope at optical wavelengths, are reduced significantly by the effects of particle coagulation. While the case with low diffusion and high nucleation rate displays a strong cloud deck and silicate feature without coagulation, the spectral appearance is dominated by molecular features when coagulation is switched on. These considerations emphasize that cloud features can only be properly interpreted by models that include coagulation.

5. Model assessment

We reflect on the achievement of our cloud model in the light of recent similar approaches. The key idea of our approach is to extend the simplicity and usability of the Ackerman & Marley (2001) model with a more physical justified cloud model, while preserving its simplicity. The Ackerman & Marley (2001) model already contained particle and vapor transport; however, it does not compute the size of the cloud particles. To proceed, a nucleation prescription is required. This we have done very crudely, simply by imposing it through ad hoc prescriptions. Alternatively, nucleation can be treated from first principles.

Photochemistry is a possible avenue for the formation of seed nuclei, which is thought to be the source of the haze as, for example, observed in Titan (Tomasko et al. 2005). Another nucleation pathway is that of homogeneous nucleation, where the nuclei seed directly form out of the vapor. The hot interiors of exoplanets characterized by thick envelopes will guarantee evaporation of any condensate at some depth. For these planets homogeneous condensation may be considered the natural way to form clouds.

These additions to the nucleation model can, in principle, render the model more physically rigorous. However they also come at a drawback. A well-known issue with the classical nucleation theory is that it mispredicts nucleation rates by many orders of magnitude (e.g., Feder et al. 1966; Tanaka et al. 2005; Horsch et al. 2008; Diemand et al. 2013). Similarly, codes that model haze formation necessarily rely on a large chemical network, with hundreds of reactions, and sophisticated radiation transport (Lavvas et al. 2008; Lavvas & Koskinen 2017; Kawashima & Ikoma 2018). Obviously, parametrizing nucleation implies that the size of the typical cloud particle no longer follows from first principles. But the transport model still addresses variations of particle concentration and size with height, which act as independent model constraints.

Another major simplification we have adopted is the characteristic particle approach (as in Ohno & Okuzumi 2017). A brief discussion on the validity and limitations of this approach can be found in Kawashima & Ikoma (2018). Recently, several studies have used CARMA[3] toward modeling clouds on exoplanets (Gao et al. 2018; Gao & Benneke 2018; Powell et al. 2018). An output of this code is the particle size distribution at any height. A possible approach is to reconstruct the entire grain size distribution from the characteristic size (cf. Helling et al. 2008 or Birnstiel et al. 2012 for disks). Nevertheless, within the ARCiS framework, solving for the particle size distribution is too computationally intensive, since we intend it to be used in future MCMC parameter searches. Altogether, we make no claim to have invented the "best" cloud model in terms of physical rigor, but one that is minimalistic, physical consistent and above all useful. Its modular approach can easily be extended to include more physical processes and its results can guide sophisticated, computationally intensive models in a complementary fashion.

6. Summary

In this paper we have studied the effects of diffusion strength and nucleation efficiency on the characteristics of clouds in exoplanet atmospheres. We have presented a relatively simple framework of cloud formation where these effects can be studied efficiently. Both the nucleation rate and the diffusion strength are key parameters in determining the properties of the cloud particles and the extent of the cloud. Since both these parameters are highly uncertain, it is important to understand their effects. We have presented simulated infrared transmission spectra for different combinations of these two parameters in a typical hot Jupiter atmosphere.

For the physical structure of the clouds we conclude the following:

- Increasing the nucleation rate results in thicker clouds of smaller particles. The high number of nuclei facilitate condensation. At the same time, the condensed mass is distributed over a larger number of particles, resulting in on average smaller particles.
- Increasing the diffusion strength results in thicker clouds. In this case, more vapor is mixed up and can condense on the nuclei. This causes simply more cloud material at each altitude and thus thicker clouds.

For the transmission spectra resulting from these structures we conclude the following:

- For increasing diffusion strength and to a lesser degree increasing nucleation rate the molecular features weaken. This is caused by increasingly thicker clouds shielding more of the gaseous atmosphere.
- For high values of the diffusion strength and nucleation rate, the solid state 10 μm silicate feature appears. This feature of the cloud particles is visible in almost all parameter settings we consider here, but is most prominent for the highest values of diffusion and nucleation because they create the thickest clouds with small particles.
- For increasing nucleation rates, that is, smaller particles, the slope of the Near-IR steepens.
- Coagulation has a significant influence on the spectral appearance of the clouds, especially in the case of high nucleation rates.

The above observational features can be used to characterize cloud particles in exoplanet atmospheres. The modeling framework we present in this paper is computationally not very demanding. We can see two very important extensions of the present model. First, the opacities obtained from the cloud model can be fed back to the physical structure, such that for example the temperature profile is obtained self-consistently (recall that we used a fixed $\kappa_{\rm IR}$ in calculating the P–T profile). Second, and maybe more important, we can use this modeling framework to include a physically motivated cloud formation model in retrieval methods. This way we can simulate the effect that clouds have on the atmospheric composition and observational features. In addition, it allows us to put observational constraints on physical parameters like the nucleation rate and the diffusion strength. This will provide a significant step forward in understanding the physical processes in exoplanet atmospheres.

Acknowledgements. C.W.O. and M.M. are grateful to Paul Mollière for providing his petitCODE to calculate the gas composition. The authors also acknowledge fruitful discussion with Christiane Helling, Paul Mollière, and Peter Woitke. C.W.O. is supported by the Netherlands Organization for Scientific Research (NWO; VIDI project 639.042.422). The research leading to these results has received funding from the European Union's Horizon 2020 Research and Innovation Programme, under Grant Agreement 776403.

[3] Community Aerosol and Radiation Model for Atmospheres.

References

Ackerman, A. S., & Marley, M. S. 2001, ApJ, 556, 872
Ascher, U. M., Mattheij, R. M. M., & Russell, R. D. 1994, Numerical Solution of Boundary Value Problems for Ordinary Differential Equations, vol. 13 (Philadelphia: SIAM)
Barstow, J. K., Aigrain, S., Irwin, P. G. J., & Sing, D. K. 2017, ApJ, 834, 50
Baudino, J.-L., Mollière, P., Venot, O., et al. 2017, ApJ, 850, 150
Birnstiel, T., Andrews, S. M., & Ercolano, B. 2012, A&A, 544, A79
Brewer, J. M., Fischer, D. A., & Madhusudhan, N. 2017, AJ, 153, 83
Chapman, S., & Cowling, T. G. 1970, The Mathematical Theory of Non-Uniform Gases. An Account of the Kinetic Theory of Viscosity, Thermal Conduction and Diffusion in Gases (Cambridge: Cambridge University Press)
Charbonneau, D., Berta, Z. K., Irwin, J., et al. 2009, Nature, 462, 891
Charnay, B., Bézard, B., Baudino, J.-L., et al. 2018, ApJ, 854, 172
Diemand, J., Angélil, R., Tanaka, K. K., & Tanaka, H. 2013, J. Chem. Phys., 139, 074309
Epstein, P. S. 1924, Phys. Rev., 23, 710
Feder, J., Russell, K. C., Lothe, J., & Pound, G. M. 1966, Adv. Phys., 15, 111
Gao, P., & Benneke, B. 2018, ApJ, 863, 165

Gao, P., Marley, M. S., & Ackerman, A. S. 2018, ApJ, 855, 86
Guillot, T. 2010, A&A, 520, A27
Helling, C., Woitke, P., & Thi, W.-F. 2008, A&A, 485, 547
Helling, C., Woitke, P., Rimmer, P. B., et al. 2014, Life, 4, 142
Henning, T., & Stognienko, R. 1996, A&A, 311, 291
Horsch, M., Vrabec, J., & Hasse, H. 2008, Phys. Rev. E, 78, 011603
Jaeger, C., Molster, F. J., Dorschner, J., et al. 1998, A&A, 339, 904
Jeans, J. 1967, An Introduction to the Kinetic Theory of Gases (Cambridge: Cambridge University Press)
Kawashima, Y., & Ikoma, M. 2018, ApJ, 853, 7
Kierzenka, J., & Shampine, L. F. 2001, ACM Trans. Math. Softw., 27, 299
Kreidberg, L., Bean, J. L., Désert, J.-M., et al. 2014, Nature, 505, 69
Kreidberg, L., Line, M. R., Bean, J. L., et al. 2015, ApJ, 814, 66
Krijt, S., Ormel, C. W., Dominik, C., & Tielens, A. G. G. M. 2016, A&A, 586, A20
Lavvas, P., & Koskinen, T. 2017, ApJ, 847, 32
Lavvas, P. P., Coustenis, A., & Vardavas, I. M. 2008, Planet. Space Sci., 56, 27
Line, M. R., Wolf, A. S., Zhang, X., et al. 2013, ApJ, 775, 137
Madhusudhan, N., Bitsch, B., Johansen, A., & Eriksson, L. 2017, MNRAS, 469, 4102
Min, M. 2017, A&A, 607, A9
Min, M., Hovenier, J. W., & de Koter A. 2005, A&A, 432, 909
Mollière, P., van Boekel, R., Dullemond, C., Henning, T., & Mordasini, C. 2015, ApJ, 813, 47
Mollière, P., van Boekel, R., Bouwman, J., et al. 2017, A&A, 600, A10
Mordasini, C. 2014, A&A, 572, A118
Mordasini, C., van Boekel, R., Mollière, P., Henning, T., & Benneke, B. 2016, ApJ, 832, 41
Morley, C. V., Fortney, J. J., Marley, M. S., et al. 2012, ApJ, 756, 172
Movshovitz, N., Bodenheimer, P., Podolak, M., & Lissauer, J. J. 2010, Icarus, 209, 616
Öberg, K. I., Murray-Clay, R., & Bergin, E. A. 2011, ApJ, 743, L16
Ohno, K., & Okuzumi, S. 2017, ApJ, 835, 261
Ohno, K., & Okuzumi, S. 2018, ApJ, 859, 34
Okuzumi, S., Tanaka, H., Takeuchi, T., & Sakagami, M.-a. 2011, ApJ, 731, 95
Ormel, C. W. 2014, ApJ, 789, L18
Powell, D., Zhang, X., Gao, P., & Parmentier, V. 2018, ApJ, 860, 18
Sato, T., Okuzumi, S., & Ida, S. 2016, A&A, 589, A15
Shampine, L. F., Muir, P. H., & Xu, H. 2006, J. Numer. Anal. Ind. Appl. Math, 1, 201
Tanaka, K. K., Kawamura, K., Tanaka, H., & Nakazawa, K. 2005, J. Chem. Phys., 122, 184514
Tomasko, M. G., Archinal, B., Becker, T., et al. 2005, Nature, 438, 765
Tsiaras, A., Waldmann, I. P., Zingales, T., et al. 2018, AJ, 155, 156
Turrini, D., Miguel, Y., Zingales, T., et al. 2018, Exp. Astron., 46, 45
Whipple, F. L. 1972, in From Plasma to Planet, ed. A. Elvius (New York: John Wiley & Sons, Inc.), 211
Woitke, P., & Helling, C. 2003, A&A, 399, 297
Yau, M. K., & Rogers, R. 1996, A Short Course in Cloud Physics (Burlington, MA: Elsevier)

Appendix A: Validation with petitCODE

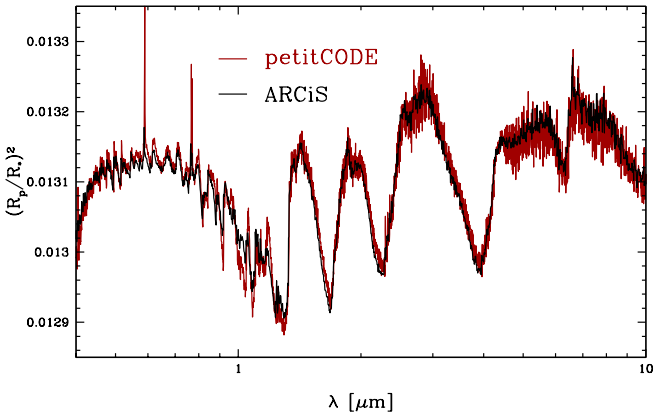

Fig. A.1. Transmission spectra for the standard model without clouds computed using petitCODE and ARCiS.

We have validated the computations performed with ARCiS with the exoplanet simulation code petitCODE (Mollière et al. 2015, 2017). The petitCODE has been extensively benchmarked in Baudino et al. (2017). We compute the transmission spectrum of the atmospheric setup from the model used here without any cloud formation. The chemistry, hydrostatic structure, molecular opacities and resulting transmission spectrum are computed both by ARCiS and petitCODE independently. The chemical equilibrium module used in ARCiS is the same as the one used in petitCODE. This module is benchmarked in Baudino et al. (2017), so here we only check the proper implementation of the module in ARCiS. Figure A.1 shows the comparison of the resulting transmission spectra. The spectra match exceptionally well at almost all wavelengths. There are some small differences in the optical part of the spectrum which can be attributed to a different Rayleigh scattering law and different opacities for TiO and VO used in both codes. These differences are irrelevant for the purpose of this paper. The petitCODE spectrum is computed at higher spectral resolution and thus shows small high frequency variations which are smoothed in the lower resolution ARCiS spectrum. We conclude that the match is excellent.